Bio-Design and Manufacturing (2025) 8:558–569
https://doi.org/10.1631/bdm.2400508

RESEARCH ARTICLE

Bioinspired magnetic microspike robot for long-term drug delivery anchoring on gliomas

Xingyue Hu[1,2,3,4] · Wen Cheng[5] · Tianyang Ma[5] · Yuting Zhou[1,3,4] · Junjian Zhou[1,3,4] · Xuechun Wang[5] · Lianqing Liu[1,3] · Anhua Wu[5] · Guannan He[6] · Niandong Jiao[1,3]

Received: 13 December 2024 / Accepted: 10 February 2025

Abstract

Treatment of intracranial gliomas has increasingly favored minimally invasive surgery, with a growing focus on leveraging microrobots for efficient drug delivery while overcoming the impact of body fluids. Inspired by honeybee stingers, this study proposed a novel microspike robot. This robot firmly adhered to the tissue surface, enabling direct drug delivery from a hydrogel on its back into the targeted tissue via microspikes. The drug delivery rate was influenced by temperature and could be controlled by an alternating magnetic field. Microrobots could be delivered rapidly through a clinical Ommaya reservoir into the postoperative cavity or ventricle of the skull. The microrobot could be actuated for adhesion and retrieval, with its motion posture and trajectory highly precisely controlled by external magnetic fields. Biological experiments confirmed the excellent biocompatibility and biosafety of the microspike robot and demonstrated its effectiveness in treating gliomas by loading unconventional therapeutic drugs. The proposed microspike robot has significant potential for long-term drug delivery to target gliomas and other future clinical applications.

Graphical abstract

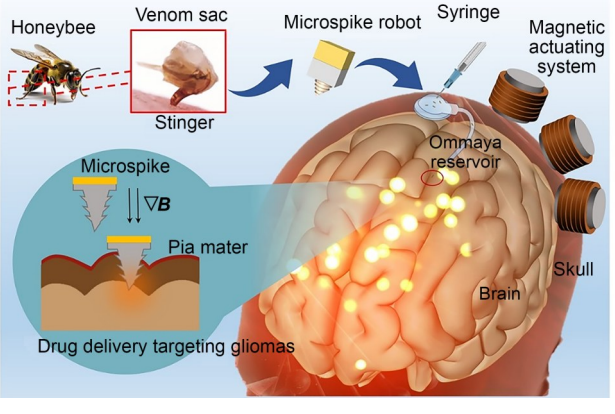

Keywords Drug delivery · Bioinspired microrobot · Magnetic microrobot · Microspike · Biocompatible materials

Xingyue Hu, Wen Cheng, and Tianyang Ma have contributed equally to this work.

✉ Anhua Wu
ahwu@cmu.edu.cn

✉ Guannan He
20092111@cmu.edu.cn

✉ Niandong Jiao
ndjiao@sia.cn

1 State Key Laboratory of Robotics, Shenyang Institute of Automation, Chinese Academy of Sciences, Shenyang 110016, China

2 College of Mechanical and Electronic Engineering, Nanjing Forestry University, Nanjing 210037, China

3 Institutes for Robotics and Intelligent Manufacturing, Chinese Academy of Sciences, Shenyang 110016, China

4 University of Chinese Academy of Sciences, Beijing 100049, China

5 Department of Neurosurgery, Shengjing Hospital of China Medical University, Shenyang 110022, China

6 Department of Anesthesiology, The First Hospital of China Medical University, Shenyang 110001, China

1 Introduction

Minimally invasive surgery for intraventricular tumors has gained prominence in clinical practice due to significant traumas associated with traditional surgical treatment [1, 2]. To minimize recurrence and postoperative complications, the timely monitoring and continuous, controlled administration of medications during postoperative care are crucial. However, many medicines are prone to inactivation and exhibit low absorption rates due to the unique location of tumors and the blood–brain barrier (BBB). Targeted drug delivery within tissues has the advantages of rapid onset, high therapeutic efficiency, and low invasiveness, making it an effective strategy for inhibiting tumor growth and promoting wound healing [3–6]. Consequently, the development of targeted drug delivery microrobots that can be deployed into ventricles through a subcutaneous Ommaya reservoir and provide long-term controlled release of therapeutic agents holds significant promise for improving postoperative outcomes in treating ventricular tumors.

Compared to subcutaneous injection needles, microspikes offer a significantly lower risk of pain and infection due to their smaller size [7–11]. Microneedle patches have been proven to be a unique carrier for various drugs, making an ideal self-administered therapeutic [10, 12, 13]. However, long-term and controlled local administration requires that microspikes adhere securely to the tissue surface [12]. In nature, honeybees can latch firmly onto invaders via their tail stingers that inject venom from venom sacs even after detachment. Honeybee stingers feature minute retrorse spines that mechanically interlock with tissues, increasing adhesion by up to 70 times [7, 14, 15]. Inspired by this unique structure and function, this design aims to replicate the ability of the honeybee stinger to achieve strong, sustained tissue adhesion in microspike-based drug delivery systems.

Smart hydrogels are recognized for their outstanding biocompatibility and mechanical properties [16–20]. In recent years, smart hydrogels have been selected by scientists as the preferred materials for medical aids, such as biological scaffolds [21–23], artificial muscles [24–26], and soft robots [27–30]. By adjusting the synthetic components of the hydrogels, these materials can be engineered to undergo reversible volume changes in response to external stimuli such as light, heat, or magnetic fields [30–34].

Magnetic fields are widely recognized as safe and effective methods for actuating microrobots due to their high precision and lack of radiation. Moreover, magnetic particles/nanowires can be induced to generate the magnetothermal effect in an alternating magnetic field (AMF), releasing heat rapidly and precisely. The heat generated by magnetic fields can be utilized to perform specific tasks on demand, or for medical therapies such as thermal therapy [35].

In this study, inspired by the stingers on the honeybee tails, an untethered microspike robot with inverted thorns was developed. Fabricated by two-photon laser printing technology, this microspike robot can achieve strong adhesion and effective local drug delivery on the surface of ventricular papilla mater tissues. Compared to traditional drug delivery microrobots, microspike robots are engineered to overcome the interference of fluid flow and firmly adhere to the biological tissue surface with sufficient adhesive force. The drug-loaded poly(N-isopropylacrylamide-co-acrylamide) (P(NIPAM-AAm)) thermosensitive hydrogel layer on the microrobot's back facilitates the continuous and direct delivery of therapeutic drugs to the targeted tissues via the internal channels of microspikes. The robot can be quickly delivered to the postoperative cavity or ventricle of the skull through hoses and minimally invasive channels. Navigated by an external magnetic field, the robot can be precisely targeted to the treatment area, where it adheres securely. Microspike robots have demonstrated excellent biocompatibility and biosafety. The long adhesion time and ability to directly inject drugs into tissues make it promising to further improve drug delivery efficiency. Treatment of mice with spontaneous gliomas has proven that the microspike robot is an effective drug delivery therapeutic tool and can expand the range of therapeutic drugs. These findings suggest that the proposed microspike robot holds significant promise for the minimally invasive treatment of gliomas and the prevention of postoperative recurrence.

2 Experimental section

2.1 Materials

NIPAM, AAm, N,N′-methylenebis(acrylamide), Rhodamine B, deionized (DI) water, the photoinitiator phenyl (2,4,6-trimethylbenzoyl) phosphine oxide (Irg. 819), and anhydrous ethanol were purchased from Sigma-Aldrich (USA). The nanoclay Laponite XLG was purchased from BYK Additives Co., Ltd. (Shanghai, China). The in vitro organs used in this study were purchased from a local market. Experimental mice were procured through legitimate experimental animal channels at China Medical University.

2.2 Preparation of the magnetic microspike robot synthesis of P(NIPAM-AAm)

Nanoclay (0.1 g) was added to 4 mL DI water as thickening and physical crosslinking agents and stirred for 4 h at 40 °C. The stirring rate was set at 1000 r/min. Subsequently, 0.392 g NIPAM monomer was added and stirred in ice water bathing for 1 h. The AAm monomer

(0.08 g) was added and continuously stirred for 1 h. N,N′-methylenebis(acrylamide) was added to the colloid as the crosslinking agent at a mass fraction of 0.5%. Subsequently, the mixed photoinitiator Irg. 819 ethanol solution (0.451 mL; 20.93 mg/mL) was added. The mixture was stirred sequentially for 10 min. Vacuum degassing was performed for 20 min to obtain a hydrogel precursor.

2.3 Fabrication of the magnetic microspike robot

The designed microspike robots were printed using a commercial two-photon polymerization (TPP) microfabrication system (Photonic Professional GT2; Nanoscribe GmbH, Germany) in galvo scan mode with a 10× objective (numerical aperture: 1.4; Zeiss, Germany). The main material of the robot adopts the commercial light curing agent IP-Q (Nanoscribe GmbH) via a 780-nm femtosecond laser under stable temperature and humidity. The femtosecond laser was 40 MW, and the slicing and hatching parameters of printing were 2 and 1 μm, respectively. Microrobots were developed in 2-acetoxy-1-methoxypropane (99.9%; Sigma-Aldrich), and the uncured part was washed away with DI water. Microspike robots were sputtered with a 20-nm nickel nanofilm coating for 30 min, with the spikes facing upward. The robot was gently peeled from the silicon substrate in water using tweezers.

The hydrogel prepolymer was dropped on the microhole side of the robot and vacuumed for 30 s. The 100-μm-thick prepolymer was spin-coated on the microhole side and cured under ultraviolet (UV) light-emitting diode (LED) light (wavelength: 365 nm) for 60 s to obtain the drug-loaded magnetic microrobot.

2.4 Magnetization and composition analysis

The magnetic microspike robot was magnetized in a high-voltage magnetization instrument. The magnetization curve of the magnetic robot was measured using a vibrating-sample magnetometer (VSM, 7404; Lake Shore, USA). The hydrogel samples were frozen in liquid nitrogen and dried in a lyophilizer (Lab-1A-80; Biocool, China). A Fourier transform infrared (FTIR) absorption spectrometer was acquired on a Thermo Nicolet iS5 instrument (Thermo Fisher, USA).

2.5 Morphology characterization

Microspike robots were freeze-dried in liquid nitrogen for 30 min before drying in a lyophilizer for 12 h. Thereafter, the freeze-dried robot was sputtered with gold and photographed under scanning electron microscopy (SEM, Hitachi SU8010; Tokyo, Japan).

2.6 Measurement of the adhesion properties

The adhesive forces of microrobots were measured by a microforce sensor (Model LSB200; FUTEK, USA). The displacement of microrobots was controlled by an electric motorized translation stage (MTS50/M-Z8; Thorlabs, Inc., USA) with a direct current (DC) servo controller (TDC001 DC motor; Thorlabs, Inc.). To measure the ability to resist fluid flow, a micropump (ISPLab02; DK Infuserek Co., Ltd., China) was used to control the fluid flow velocity within the simulated blood vessels.

2.7 Magnetic actuation equipment for microrobots

The magnetic microrobot was actuated in a self-customized five-coil electromagnetic system using an inverted microscope. The magnetic field was controlled by the programmed software via LabVIEW. AMF was generated by a high-frequency induction heating machine (SPG-10A-II; Shenzhen Shuangping Power Supply Technologies Co., Ltd., China).

2.8 Drug loading and release

The fluorescent particle Rhodamine B (1 mg/mL; maximum absorption wavelength of approximately 554 nm) was dissolved in the hydrogel precursor as a simulated drug. Robots loaded with fluorescent drugs were observed for drug-loading effects via an eclipse Ti microscope (TIE; Nikon, Tokyo, Japan). The drug-release solution from microrobots was regularly sampled and measured via a UV– Visible spectrophotometer (LAMBDA1030; PerkinElmer, USA). The robot adhered to the gelatin methacryloyl (GelMA) hydrogel block of the simulated tissue, and the amount of fluorescence resulting from the drug delivery diffusion was characterized with ImageJ.

2.9 In vivo biosafety verification

Eight-week-old male mice (C57BL/6; Beijing Vital River Laboratory Animal Technology, China) were purchased to confirm the biocompatibility of microspike robots. Mice were fixed on a stereotactic apparatus (71000; Shenzhen RWD Life Science and Technology, China), and their skulls were exposed and windowed with a microcranial drill. Microrobots were gently placed, and the skin was sutured. Throughout the process, isoflurane (Shenzhen RWD Life Science and Technology) was used to anesthetize mice. Mice were subsequently observed regularly, and their body weights were measured. After 10 d, mice were euthanized to obtain vital organs.

2.10 Hematoxylin-and-eosin (H&E) staining

After mice were euthanized, the brain, heart, liver, spleen, lungs, and kidneys were extracted and fixed in paraformaldehyde (Sigma-Aldrich). After embedding in paraffin, 4-μm-thick tissue sections were cut onto slides. Deparaffinization and rehydration were then performed. Next, the slides were treated with hematoxylin solution for 5 min and eosin solution for 60 s. Finally, the slides were covered with resin.

2.11 Mouse model and implantation of the microrobot

Mice were group-housed in ventilated cages under controlled temperature and humidity with a 12-h light/dark cycle. Every animal was randomized by body weight before the experiments. For the orthotopic mouse model, 2×10^4 sleeping beauty (SB) mouse glioma sphere cells were stereotactically injected into five-week-old male BALB/c nude mice to establish an SB-bearing murine spontaneous glioma model [36]. The injection coordinates were 2.0 mm to the right of the midline and 2.0 mm posterior to the anterior fontanel at a depth of 2.0 mm. When severe neurological symptoms were observed in a mouse, in vivo imaging was conducted to confirm the success of the model construction. On the following day, microrobots were implanted at the same coordinates. For the single large-dose treatment group, 2 μg/g doxorubicin (DOX) was directly injected intracranially into mice. For the small-dose multiple-injection group, 0.67 μg/g DOX was administered intracranially daily for six consecutive days, with the total duration and cumulative dose consistent with the other groups. After a 3-d interval, a second implantation of microrobots was performed. Three days later, another round of in vivo imaging of mice was conducted. In vivo fluorescence imaging was performed using the LB 983 Animal In Vivo Imaging System (Berthold Technologies, Germany). After this, mice were euthanized with carbon dioxide for histopathological section preparation. Changes in body weight throughout the process were recorded, and data were analyzed via GraphPad Prism.

2.12 Statistical analysis

All measurements were performed three to five times per experiment. Quantitative data were presented as mean± standard deviation. Data were analyzed via Origin 2022 (OriginLab Corp., MA, USA). The level of statistical significance was set at $p<0.05$. Error bars represent the standard deviation.

3 Results and discussion

3.1 Design and fabrication of the microspike robot

To mimic the tail stinger structure of honeybees that can anchor for a long time and the venom sac that can deliver venom, two-photon polymerization was used to fabricate a tail stinger with retrorse spines and a drug delivery channel, while a drug-loaded hydrogel was employed as the "venom sac." To ensure a stable mechanical structure in physiological solutions, the epoxy resin IP-Q precursor was scanned layer by layer according to a programmed femtosecond laser trajectory with a layer thickness of 5 μm. Subsequently, a high-resolution 3D microspike structure with the designed shape was generated in the developing solution for 20 min (Fig. 1a1). After rinsing and drying the structure, a metal coating of nickel and gold was applied to the structural side of the microrobot through magnetron sputtering for 30 min, separately (Fig. 1a2). The robot was then gently lifted from the silicon substrate in water using tweezers. Next, the P(NIPAM-AAm) precursor synthesized in the experimental section was dropped onto the micropore side of the robots and vacuumed for 30 s to draw the drug-loaded hydrogel precursor into the microporous structure. Subsequently, the excess hydrogel was evenly coated on the backside of the structural block by spin-coating for 100 μm. Finally, the hydrogel was cured by UV LED light irradiation for 60 s to obtain the drug-loaded magnetic microspike hydrogel (Fig. 1a3).

SEM images revealed that the printed robot body features clearly defined microspikes with inverted structures, and these microspikes contained hollow drug-loaded channels (Figs. 1b1 and 1b2). Drug-loaded hydrogels exhibited a dense porous structure that provides sufficient storage space for drug particles (Fig. 1b3). After the drug-loaded hydrogel was attached to the microspike robot, the distinct bilayer structure of the microrobot remained apparent (Fig. 1b4). A side view shows that the drug-loaded hydrogel layer securely adhered to the back of the microspike robot. Correspondingly, the energy-dispersive spectroscopy image clearly depicts the distribution of the nickel metal coatings on the robot's microspike surface (Fig. 1c). The fluorescently stained hydrogel can be used to simulate the drug-loaded hydrogel, demonstrating successful infiltration into the micropuncture holes. In the side view, fluorescence intensity was notably greater in the microspikes than in other areas, reflecting the presence of the hydrogel within the microspike channels (Fig. 1d). Furthermore, the hysteresis loop of microrobots was measured (Fig. 1e). The magnetized microrobot exhibited significantly stronger hysteresis than its residual and saturation magnetization levels before magnetization. The illustration shows an enhanced saturation magnetization even after magnetization. Therefore, the

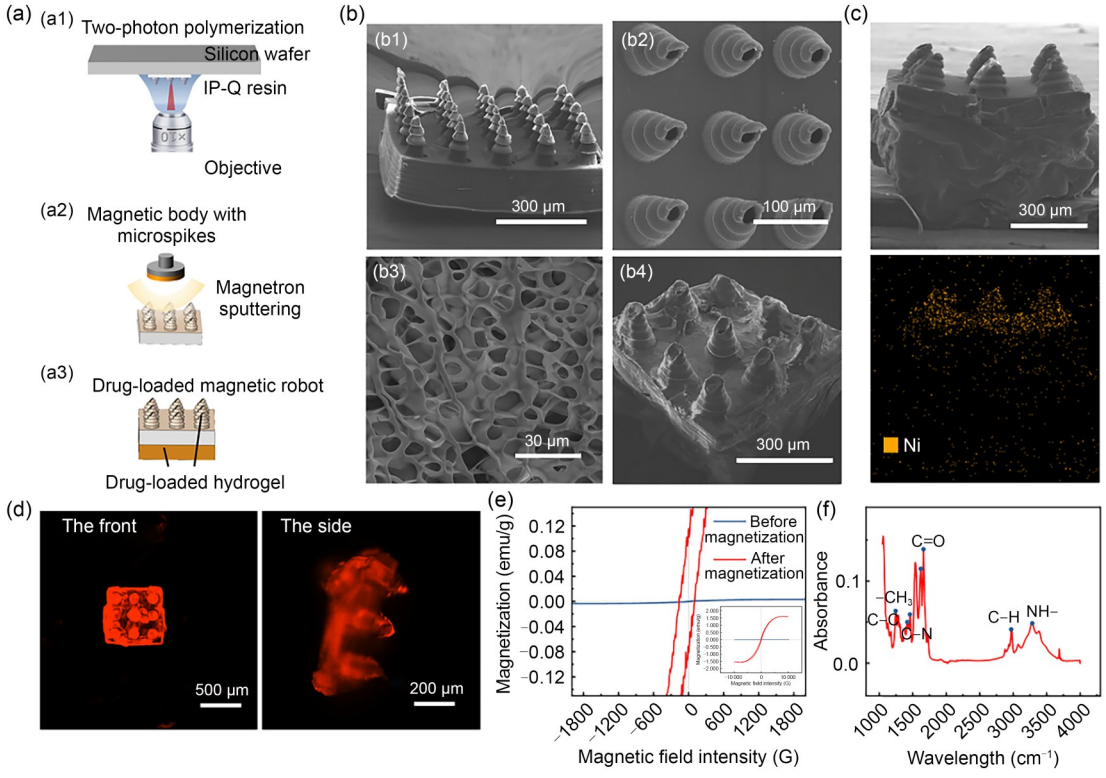

Fig. 1 Fabrication and characterization of microrobots. (a) Production process of magnetic microspike robots: (a1) printing the model of the microspike robot using the TPP system; (a2) sputtering metal onto the surface of the microspike robot model; (a3) spin-coating and adsorbing the drug-loaded hydrogel onto the back of the microspike robot. (b) SEM images of microspike robots: (b1) overall morphology; (b2) hollow microspike with inverted spikes; (b3) morphology of the hydrogel; (b4) the microspike robot integrated with a drug-loaded hydrogel. (c) Side view and corresponding energy spectrum of the microspike robot. (d) Fluorescence images of the front and side of the microspike robot. (e) Hysteresis loop of microrobots (1 emu/g=1 A·m^2/kg; 1 G=10^{-4} T). (f) FTIR spectrum of the hydrogel

magnetized robot can be effectively actuated by an external magnetic field. The presence of methyl and acrylamide in the hydrogel layer was confirmed by the absorption peak in the FTIR absorption spectrum (Fig. 1f).

3.2 Adhesion ability of the microspike robot

The microrobot leverages geometric frictional resistance to achieve large adhesion on the tissue surface so that it can adhere firmly to the treatment area in the constantly circulating cerebrospinal fluid (CSF). The adhesive force generated by the individual microspike robot sheets of various specifications was measured via microforce sensors (Fig. 2a; Figs. S1 and S2 in the supplementary information). The dimensions and morphology of microspike robots are provided in Fig. S2 (supplementary information). The adhesive force can be calculated through the force curve. The experimental results indicated that the adhesive force is proportional and inversely proportional to the number and diameter/height of the robot microspikes, respectively (Fig. 2b). In contrast, if the diameter/height of the robot is too small, the microspikes are prone to breaking, which could compromise the operation and application of the microrobot.

Given the continuous circulation of the CSF in the brain, there is a need to verify the stability of the robot's anchoring. Robots that adhere firmly to the target area are a prerequisite for improving drug delivery efficiency. Through magnetic resonance imaging plain scans, Wei et al. reported that the maximum flow rate of the CSF in the subarachnoid space reaches 0.5 cm/s [37]. In addition, Young's modulus of the GelMA hydrogel under various UV curing times was compared to that of mouse brain tissue to assess material compatibility. Among them, the GelMA hydrogel cured for 4 s exhibited mechanical properties closely matching those of biological brain tissue and was selected as a simulated tissue for subsequent experiments (see Note S2 in the supplementary information). The GelMA hydrogel was cured on the inner wall of a silica gel catheter (inner diameter: 3 mm) to simulate the brain tissue, and microspike robots were randomly attached to the inner wall of the simulated blood vessel (Fig. 2c). The detachment of microrobots was tested at different flow rates. Experimental results revealed that microrobots remained securely attached even at flow rates 20 times higher than the maximum CSF flow rate. In contrast, microrobots that are not anchored to the tissue surface with microspikes are easily dislodged by the

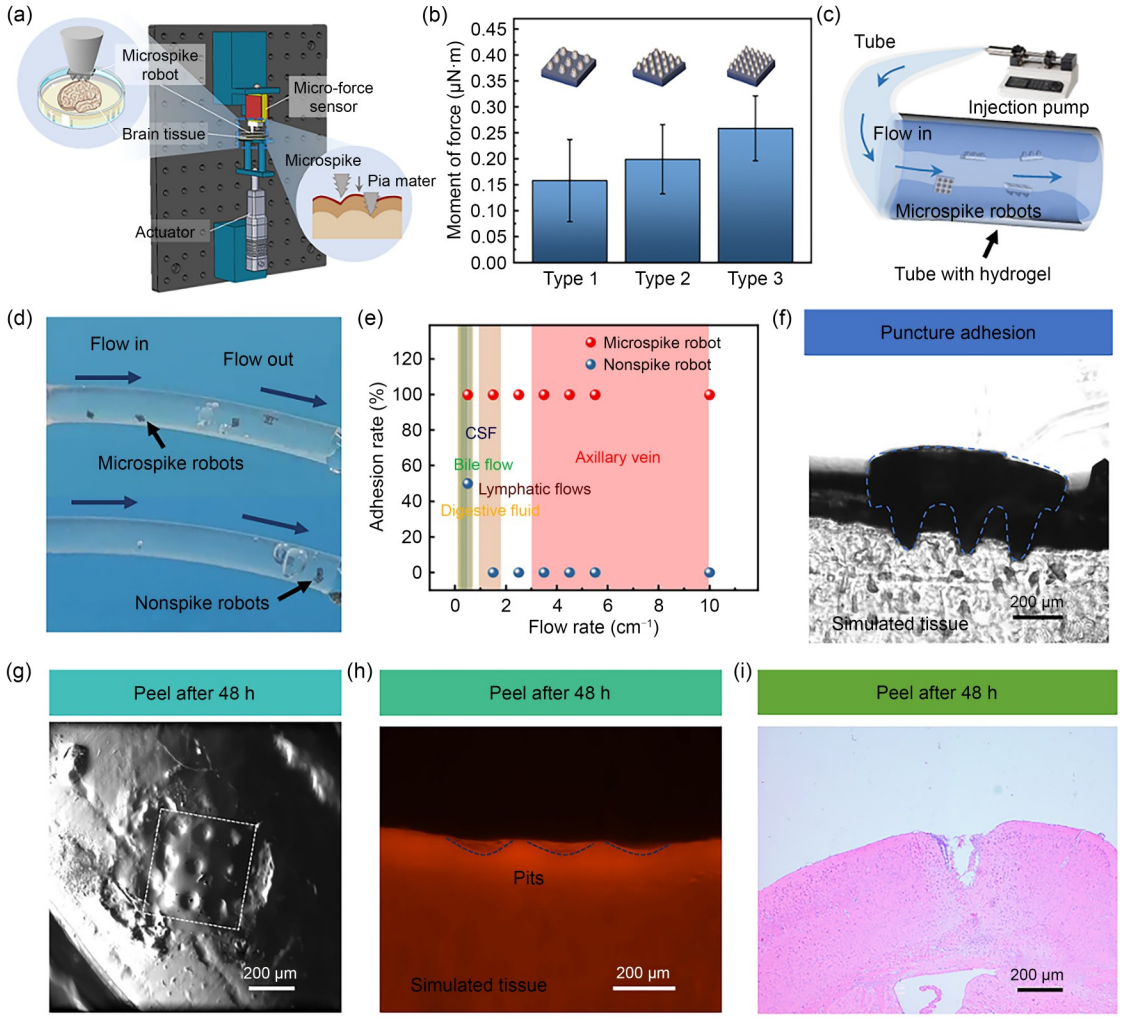

Fig. 2 Characterization of the adhesion of microspike robots. (a) Measurement device used to evaluate the adhesion of microrobots. (b) Adhesion ability of the microspike robot. (c) Measurement schematic diagram of the resistance of the microspike robot to liquid flow. (d) Adhesion performance of microspike robots compared to that of nonspike robots in fluidic environments. (e) Comparison of the adhesion retention rates of microspike and nonspike robots across various internal fluids at different flow rates. (f) Side-view optical image of the microspike robot adhering to the simulated tissue. (g) Pits formed on the simulated tissue surface after the microspike robot was peeled off. (h) Fluorescence image of pits formed after peeling. (i) H&E staining of mouse brain tissue after the microspike robot was peeled off. Data in (b) are expressed as mean±standard deviation (n=5)

fluid flow (Fig. 2d; Video S1 in the supplementary information). These findings proved that microrobots can adhere robustly to the vast majority of body fluids [38–41]. Furthermore, microrobots maintained stable adhesion and intravenous administration within the vena cava vessels (Fig. 2e). The strong adhesion capabilities of microrobots enable them to remain anchored in the target area for extended periods, providing favorable conditions for long-term targeted drug release.

Figure 2f shows a microscopic optical image of the microrobot adhering to the simulated tissue surface via its microspikes. After 48 h adhesion, the microspike robot was peeled off, revealing corresponding pits on the simulated tissue surface (Fig. 2g). Fluorescence imaging revealed that the depth of these pits was <50 μm (Fig. 2h). The microrobot was attached to the surface of a mouse brain for 48 h, after which the tissue was sectioned and subjected to H&E staining. Results revealed that only minimal cell damage occurred in the pits formed by the microspikes, and no signs of inflammation were observed (Fig. 2i). These results suggested that microspike robots do not cause significant harm to brain tissue, supporting their safety and potential for medical applications.

3.3 Controllable drug release of the microspike robot

To achieve controllable drug-release efficiency, thermosensitive hydrogels were used as drug carriers. In Fig. 3a, the hydrogel underwent reversible contraction and swelling

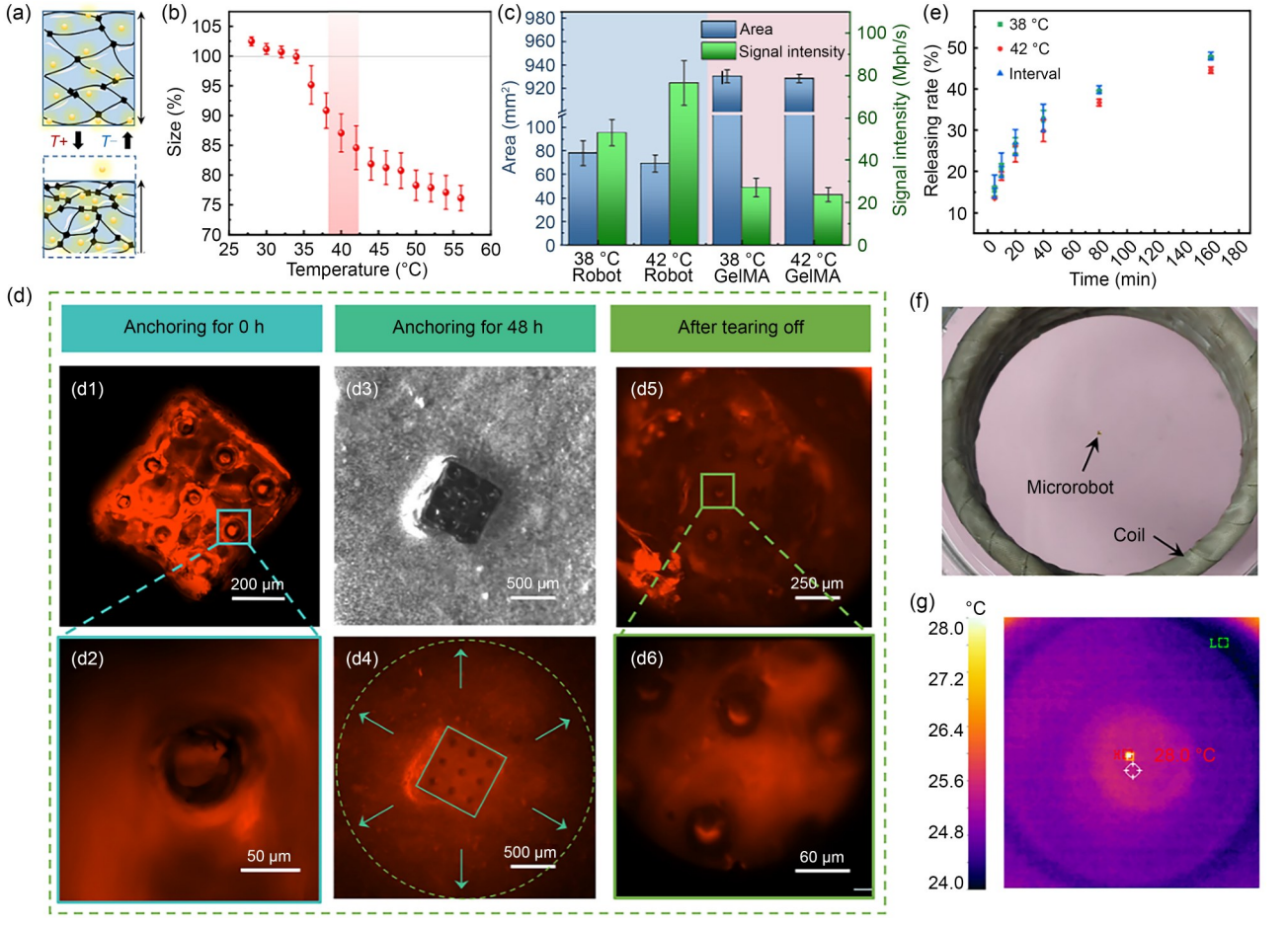

Fig. 3 Drug delivery by microspike robots. (a) Schematic diagram of the drug-loaded thermosensitive hydrogel. (b) Relationship between the thermosensitive hydrogel size and temperature changes. (c) Area and signal intensity per unit area of the drug-loaded thermosensitive hydrogel on microspike robots and the simulated tissue after being attached for 48 h at 38 °C and 42 °C. (d) Fluorescence images of the microrobot drug delivery process. Fluorescence imaging of the robot after anchoring for 0 h (d1) and a magnified view of its microspikes (d2). Optical image (d3) and diffused fluorescence imaging (d4) of the microspike robot after anchoring for 48 h. Fluorescence image of the simulated tissue after tearing the robot off (d5) and a magnified view of the microspike pits (d6). (e) Drug-release rates at different temperatures. (f) Optical image of the microrobot heated by a high-frequency AMF. (g) Thermal infrared (IR) imaging of a microrobot heated by a high-frequency AMF. Data in (b, c, e) are expressed as mean±standard deviation (n=5)

in response to temperature changes. The reversible expansion and contraction of the hydrogel networks affect the drug particle delivery. Measurement results revealed that the hydrogel volume decreased gradually from the swollen state as the temperature increased. Among them, significant volume differences were observed at body temperatures of 38 and 42 °C (Fig. 3b). Accordingly, when the fluorescent drug-loaded microrobot was exposed to an ambient temperature of 42 °C, the surface area of the drug-loaded hydrogel was smaller than that at 38 °C, resulting in an enhanced fluorescence signal per unit area on the robots (Fig. 3c; Fig. S3 in the supplementary information). The drug-loaded microspike robots were attached to the simulated tissue surface for 48 h. After adhesion, in the simulated tissue GelMA, the fluorescence diffusion area at 38 °C was not much different from that at 42 °C, but the fluorescence intensity per unit area was higher than the latter. The fluorescence images showed that the drug-loaded hydrogel in the robot's microspike channels is clearly visible upon adhesion, whereas no fluorescent signal appears around the microrobot (Figs. 3d1 and 3d2). After 48 h adhesion, the fluorescence signal diffused around the microrobot, indicating that the drug particles were delivered to the simulated tissue (Figs. 3d3 and 3d4). This diffusion is driven by the osmotic pressure of the drug, causing the drug particles to move from the drug-loaded layer on the back to the tissue interior. Upon peeling off the robot, detectable fluorescence signals were observed within the simulated tissue, with high concentrations in the pits formed by the microspike channels (Figs. 3d5 and 3d6). Compared to the nonspike robots in Note S3 (supplementary information), the hollow channels inside the microspikes of the microspike robot were proven crucial for effective direct drug delivery. The drug-release efficiency of the

robot was measured, revealing that it continuously released drugs over a 3-h period, with the release rate at 42 °C being lower than that at 38 °C (Fig. 3e). These findings demonstrated that reducing the hydrogel's mesh size by increasing the temperature reduces the drug delivery rate. The survival rate of brain gliomas in the drug solution released by the drug-loaded robot at different temperatures also validated this conclusion (Fig. S4 in the supplementary information).

Using AMF, remote and precise temperature control can be achieved. The coated robot was placed inside the spiral coil of the high-frequency AMF generator (Fig. 3f). Owing to the hysteresis effect, the surface gold particles and nickel nanowires generate heat when exposed to a high-frequency AMF. A thermal IR imager revealed that heating at a frequency of 330 kHz and a current of 0.3 A for 1 min resulted in a 4 °C increase in the microrobot's temperature compared to the ambient temperature (Fig. 3g). This demonstrated that the precise temperature control of the microrobot could be achieved through an external high-frequency AMF. Unlike traditional IR laser irradiation, this method minimizes thermal damage to the surrounding nontarget areas and is suitable for applications in enclosed areas. Notably, alternating the robot's temperature by switching on and off within 1-min intervals increased the drug-release efficiency (Fig. 3e). This observation suggested that further research into optimizing the solution is warranted in future studies.

3.4 Delivery, actuation, and retrieval of the microspike robot

Utilizing minimally invasive channels for the rapid and accurate delivery of untethered microspike robots, it is possible to administer anticancer drugs effectively to brain tissues, thereby enabling efficient treatment and prevention of postoperative glioma recurrence. The delivery and retrieval of microspike robots within the skull are facilitated through the medical Ommaya reservoir and external magnetic actuation fields. The corresponding medical tube of the clinical Ommaya reservoir is inserted into the brain through minimally invasive channels or the postoperative cavity, with the tube outlet positioned at the targeted position. The Ommaya reservoir is then secured to the skull's outer surface, which is a common medical procedure. Microspike robots, marked by the red circle and suspended in physiological saline, were injected into the reservoir through a syringe (Fig. 4a). As physiological saline is gradually injected, microrobots are efficiently and rapidly delivered through the tube connected to the reservoir into the skull model, reaching deep-targeted areas with minimal tissue damage. This

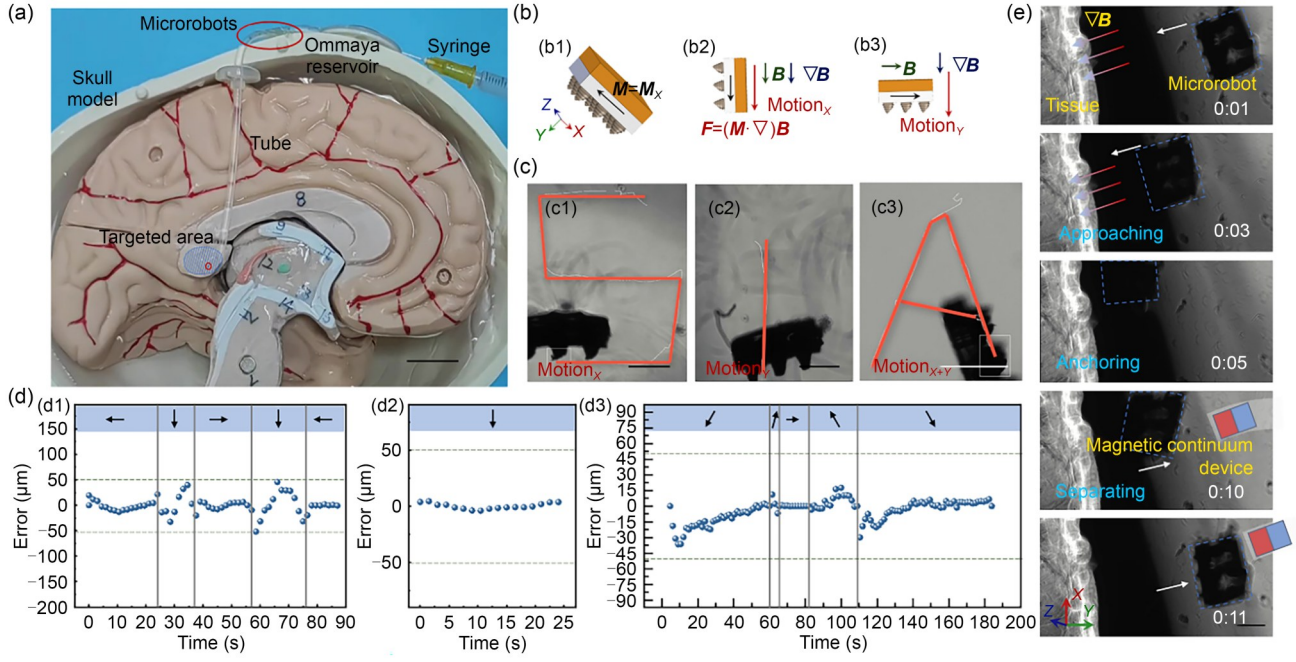

Fig. 4 Delivery, actuation, and recycling of microrobots in the model. (a) Optical image demonstrating the rapid delivery of microrobots through a medical Ommaya reservoir and tube. The red circles mark the positions of microspike robots. Scale bar: 1 cm. (b) Schematic diagram of the magnetic actuation microrobots. (b1) Magnetization direction of the microrobot. The microrobot generates Motion$_X$ in the direction parallel to the magnetization (b2) and Motion$_Y$ in the direction perpendicular to the magnetization (b3) under the actuation magnetic fields. $\boldsymbol{B}$ is the magnetic field, and $\nabla \boldsymbol{B}$ is the magnetic field gradient. (c) Micro-optical images showing the microrobot's path along "S" in the postures of Motion$_X$ (c1), "I" in the postures of Motion$_Y$ (c2), and "A" in the postures of a combination of Motion$_X$ and Motion$_Y$ (Motion$_{X+Y}$) (c3) during actuation within an electromagnetic system. Scale bar: 200 μm. (d) Errors between the actual paths of the microrobot and the given trajectories of "S" (d1), "I" (d2), and "A" (d3). (e) Process of magnetic actuation for the adhesion and detachment of microrobots. Scale bar: 200 μm

method enables the sustained, rapid, and accurate delivery of microspike robots, optimizing therapeutic outcomes.

Furthermore, the robot can be more accurately delivered to the targeted tumor location with the navigation of an external magnetic field. The magnetized microspike robot has a magnetization direction aligned along a single edge ($\boldsymbol{M}=\boldsymbol{M}_X$) to adopt various motion postures in the electromagnetic actuation system (Fig. S5 in the supplementary information). Figure 4b illustrates two distinct motion postures: one along the magnetization direction X (Motion$_X$) and the other perpendicular to it, along the Y direction (Motion$_Y$). Motion$_X$, where the actuating magnetic field $\boldsymbol{B}$ direction and the magnetic field gradient $\nabla\boldsymbol{B}$ direction are parallel to the magnetization direction, allows microspike robots to navigate through narrower channels. Motion$_Y$, where the actuating magnetic field $\boldsymbol{B}$ direction is parallel to the magnetization direction but the magnetic field gradient $\nabla\boldsymbol{B}$ direction is perpendicular to the magnetization direction, provides the microspike robot with pressure to adhere to the tissue surface. In Figs. 4c1–4c3, the micro-optical images display the robot moving along the trajectories "S," "I," and "A" in Motion$_X$, Motion$_Y$, and their combination (Motion$_{X+Y}$), respectively. The trajectory errors of microrobots were tracked and analyzed at various stages throughout the actuation process. Results showed that the motion error remained within 50 μm, which is approximately one-tenth of the robot's body length under any motion mode (Fig. 4d). Among them, larger errors occur at the turning points. Therefore, microrobots actuated by magnetic fields exhibit high control accuracy. In addition, the motion speed that the robot can reach was observed and recorded on a macroscopic scale, proving that the microrobot can be actuated in the normally flowing CSF (Fig. S6 and Video S3 in the supplementary information).

In addition, Fig. 4e illustrates the adhesion and detachment process of microspike robots. Actuated by the gradient field generated by the electromagnetic system, the microrobot moves towards the simulated tissue and ultimately adheres to its surface. This provides a foundation for the ability of microspike robots to achieve direct drug delivery within tissues via microspikes. The magnetic attraction at the magnetic head end of the magnetic continuum device subsequently facilitates the detachment and retrieval of the microspike robot (Video S4 in the supplementary information). This demonstrated that the microspike robot can achieve adhesion and retrieval through external magnetic fields.

3.5 In vivo biomedical applications of the microspike robot

The premise for the long-term application of microrobots in the body is to ensure that the robots have excellent biocompatibility. The microspike robot composed of a metal-coated resin body and a drug-loaded hydrogel was cocultured with C2C12 mouse myogenic cells (Fig. S7 in the supplementary information). Experimental results indicated that the cells could survive on the hydrogel surface and the magnetic robot and proliferate gradually within 48 h with a survival rate exceeding 90%. These results confirmed that the microrobot has good biocompatibility. To further investigate the potential clinical applications of microrobots, microspike robots were implanted into mouse brains undergoing craniotomy surgery (Figs. S8 and S9a in the supplementary information). Craniotomy was performed via a stereotactic apparatus and an automatic cranial drill, followed by the attachment of microspike robots to the outer surface of the brain tissue through micropores and subsequent wound stitching. Their physiological responses showed only a negligible difference between the weight of the group implanted with microspike robots and that of the healthy group (Fig. S9b in the supplementary information). H&E staining revealed no inflammation in the main organs of the craniotomy surgery or robot implantation group, with only a slight inflammatory reaction at the surface injury site of the treated brain tissue compared to that of healthy mice (Fig. S9c in the supplementary information). This finding indicated that the application of microrobots for brain therapy does not introduce additional safety risks. Overall, the above results demonstrated the biocompatibility and biosafety of microspike robots, which support their potential for clinical applications.

Traditional cancer treatment drugs cannot penetrate the BBB, which limits the range of drugs that can be used to treat gliomas through conventional peripheral injection. The microspike robot, which is designed to carry drugs and is directly injected into tissues via its microspikes, holds the promise of expanding the range of drug options. DOX cannot cross the BBB, posing a significant challenge for treating brain tumors such as gliomas. To evaluate the efficacy of microrobots loaded with DOX in limiting tumor progression, we first implanted these microrobots into mouse brains confirmed to carry orthotopic luciferase SB (SB-Luc) tumors. In Fig. 5a, SB-Luc cells were intracranially injected into mouse brains, which were then raised for 14 d. On Day 15, microspike robots loaded with DOX (2 μg/g) were implanted and allowed to adhere to mouse brains via their spikes. To maintain an effective DOX dose, a second drug-loaded robot was implanted 3 d later. After the final implantation, tumors in mouse brains were subjected to fluorescence imaging and measured on the 21st day. In Fig. 5b, significant fluorescence of the tumors was observed after 14 d of incubation, indicating that spontaneous murine tumors were successfully constructed in mouse brains. The group implanted with empty microrobots and the control group presented increased tumor fluorescence on Day 21. In contrast, the group treated with DOX-loaded microrobots

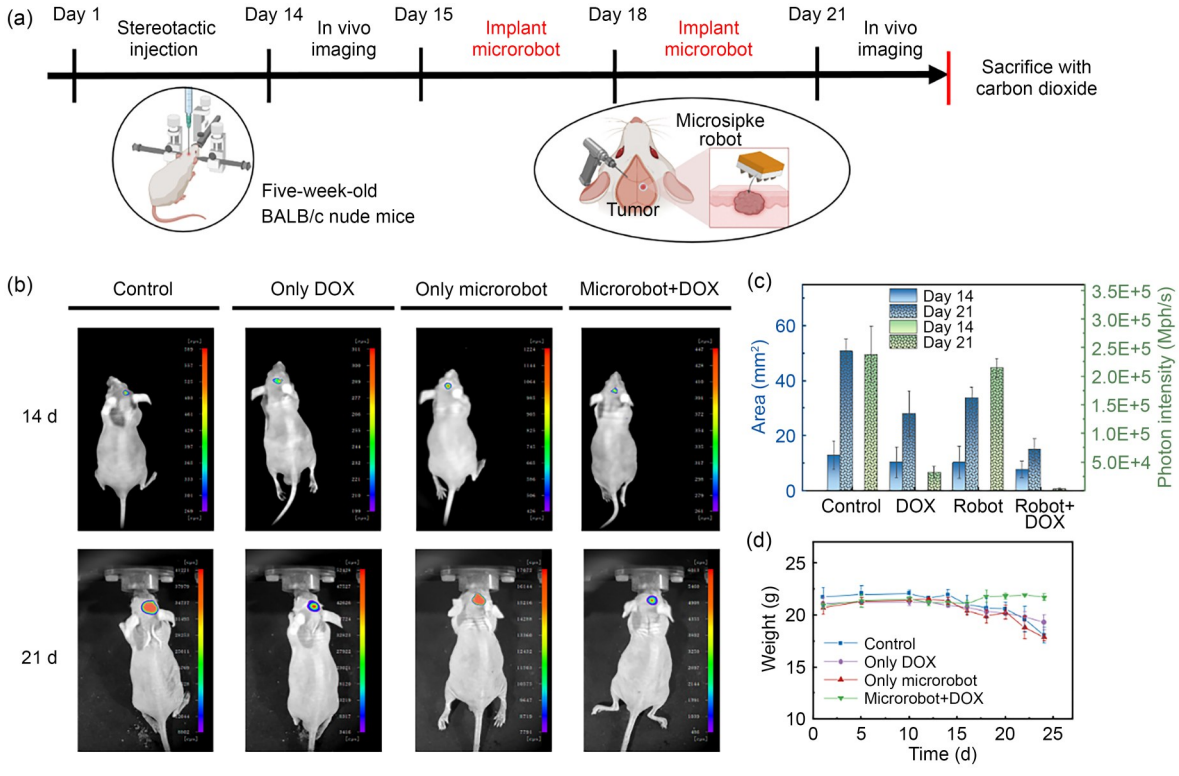

Fig. 5 Treatment of glioma in mice via drug-loaded microspike robots. (a) Experimental procedure for culturing glioma-bearing mice and treating them with drug-loaded microspike robots. (b) Fluorescence imaging of glioma regions in mouse brains. (c) Quantification of the fluorescence areas and total photon intensities of the glioma regions in mouse brains. (d) Body weight measurements of mice throughout the treatment period. Data in (c, d) are expressed as mean±standard deviation (n=5)

exhibited significant tumor suppression. Notably, direct intracerebral injection of the same DOX dose into mice bearing gliomas resulted in mortality (Fig. S10 in the supplementary information). However, when an equivalent dose of the drug was administered directly into the mouse brain in multiple injections, tumor growth could still be observed. In Fig. 5c, the fluorescence area and total photon intensity of the glioma region were calculated in each group of mice. These results indicated that DOX-loaded microspike robots can effectively inhibit glioma growth and reduce tumor size. This highlighted that the microspike robot is an effective carrier tool for glioma treatment, significantly expanding the range of therapeutic drug options.

In addition, the body weights of mice were monitored and recorded throughout the rearing process (Fig. 5d). In the control group and the group implanted with empty robots, the body weights did not increase over time but instead gradually decreased. Mice that received multiple direct injections of the drug also showed a gradual decrease in body weight, indicating that directly injecting drugs that cannot cross the BBB into the brain multiple times could be harmful to mice. In contrast, mice gained a small amount of weight after drug-loaded robots were implanted, indicating that drug-loaded robots had a therapeutic effect on tumors. The observed trend in body weight changes further supported the efficacy of drug-loaded robots in treating gliomas.

4 Conclusions

In summary, inspired by the natural design of honeybees, a microspike robot with inverted spines was fabricated via two-photon laser printing. The microspike structure on the robot surface ensures stable adhesion to the target area within flowing body fluids while minimizing damage to biological tissues. This study demonstrated that the motion mode and trajectory of microrobots with magnetic coatings can be precisely controlled through external electromagnetic systems. Future research combining systems with closed-loop control could further increase motion accuracy.

In addition, the hollow structure of microspike robots allows for the continuous and direct delivery of drugs encapsulated in the hydrogel to the target tissues. Traditional drug delivery systems for microrobots rely primarily on surface absorption and blood circulation, often limiting their efficiency. In contrast, microspike robots described in this study provide a more direct and effective approach by delivering drugs directly to targeted tissues (Fig. S11 in the supplementary information). The efficiency of this drug

delivery can be precisely controlled through an external AMF applied to the metal coating on the microspike surface. Remarkably, there is potential to further accelerate drug delivery rate, which is a promising area for future research. The synthetic materials used in microspike robots exhibited excellent biocompatibility, as demonstrated in mouse experiments. These studies showed that microspike robots can effectively treat gliomas, significantly expanding the range of therapeutic drug options. Collectively, these features indicated that microspike robots have practical value in medical treatment and postoperative care.

Supplementary Information The online version contains supplementary material available at https://doi.org/10.1631/bdm.2400508.

Acknowledgements This work was supported by the National Key R&D Program of China (No. 2023YFB4705600), the National Natural Science Foundation of China (Nos. U23A20342, 62273331, 61925307, and 61821005), the CAS Project for Young Scientists in Basic Research (No. YSBR-036), and the CAS/SAFEA International Partnership Program for Creative Research Teams.

Author contributions XYH, LQL, AHW, and NDJ participated in conceptualization. XYH, YTZ, and JJZ completed the experiments, software, and data curations. WC, TYM, XCW, and AHW provided support in the animal studies. XYH and TYM drafted the paper. NDJ contributed to writing—review and editing. GNH, LQL, AHW, and NDJ were involved in methodology, supervision, and funding acquisition.

Declarations

Conflict of interest The authors declare that they have no conflict of interest.

Ethical approval The experimental protocol was approved (No. 2023PS1153K) by the Ethics Committee of Shengjing Hospital, which is affiliated with China Medical University. Animal experiments were conducted following the guidelines of the China Medical University Animal Care and Use Committee and further approved by the Institutional Review Board of Shengjing Hospital, affiliated with China Medical University.

Data availability The data that support the findings of this study are available from the corresponding authors upon reasonable request.

References

1. Dupont PE, Nelson BJ, Goldfarb M et al (2021) A decade retrospective of medical robotics research from 2010 to 2020. Sci Robot 6(60):eabi8017. https://doi.org/10.1126/scirobotics.abi8017
2. Huang XS, Yang JB, Huang S et al (2022) Minimally invasive technology for continuous glucose monitoring. Bio-Des Manuf 5(1):9–13. https://doi.org/10.1007/s42242-021-00176-x
3. Hu SS, Pei XB, Duan LL et al (2021) A mussel-inspired film for adhesion to wet buccal tissue and efficient buccal drug delivery. Nat Commun 12(1):1689. https://doi.org/10.1038/s41467-021-21989-5
4. Wang ZJ, Yang ZP, Jiang JJ et al (2022) Silk microneedle patch capable of on-demand multidrug delivery to the brain for glioblastoma treatment. Adv Mater 34(1):e2106606. https://doi.org/10.1002/adma.202106606
5. Pané S, Puigmartí-Luis J, Bergeles C et al (2019) Imaging technologies for biomedical micro- and nanoswimmers. Adv Mater Technol 4(4):1800575. https://doi.org/10.1002/admt.201800575
6. Xu KC, Ko SH, Chen J (2024) Advances in wearable and implantable bioelectronics for precision medicine. Bio-Des Manuf 7(4):383–387. https://doi.org/10.1007/s42242-024-00302-5
7. Han D, Morde RS, Mariani S et al (2020) 4D printing of a bioinspired microneedle array with backward-facing barbs for enhanced tissue adhesion. Adv Funct Mater 30(11):1909197. https://doi.org/10.1002/adfm.201909197
8. Zhang XX, Fu X, Chen GP et al (2021) Versatile ice microneedles for transdermal delivery of diverse actives. Adv Sci 8(17):e2101210. https://doi.org/10.1002/advs.202101210
9. Yao DR, Kim I, Yin SK et al (2024) Multimodal soft robotic actuation and locomotion. Adv Mater 36(19):e2308829. https://doi.org/10.1002/adma.202308829
10. Wu YD, Dong XG, Kim JK et al (2022) Wireless soft millirobots for climbing three-dimensional surfaces in confined spaces. Sci Adv 8(21):eabn3431. https://doi.org/10.1126/sciadv.abn3431
11. Bao QD, Zhang XT, Hao ZK et al (2024) Advances in polysaccharide-based microneedle systems for the treatment of ocular diseases. Nanomicro Lett 16(1):268. https://doi.org/10.1007/s40820-024-01477-3
12. Fan L, Zhang XX, Nie M et al (2022) Photothermal responsive microspheres-triggered separable microneedles for versatile drug delivery. Adv Funct Mater 32(13):2110746. https://doi.org/10.1002/adfm.202110746
13. Zhang XX, Chen GP, Bian FK et al (2019) Encoded microneedle arrays for detection of skin interstitial fluid biomarkers. Adv Mater 31(37):e1902825. https://doi.org/10.1002/adma.201902825
14. Ling JT, Song ZH, Wang JR et al (2017) Effect of honeybee stinger and its microstructured barbs on insertion and pull force. J Mech Behav Biomed Mater 68:173–179. https://doi.org/10.1016/j.jmbbm.2017.01.040
15. Chen ZP, Lin YY, Lee W et al (2018) Additive manufacturing of honeybee-inspired microneedle for easy skin insertion and difficult removal. ACS Appl Mater Interfaces 10(35):29338–29346. https://doi.org/10.1021/acsami.8b09563
16. Hu XY, Ge ZX, Wang XD et al (2022) Multifunctional thermomagnetically actuated hybrid soft millirobot based on 4D printing. Compos Part B Eng 228:109451. https://doi.org/10.1016/j.compositesb.2021.109451
17. Gaharwar AK, Peppas NA, Khademhosseini A (2014) Nanocomposite hydrogels for biomedical applications. Biotechnol Bioeng 111(3):441–453. https://doi.org/10.1002/bit.25160
18. Xue X, Hu Y, Deng YH et al (2021) Recent advances in design of functional biocompatible hydrogels for bone tissue engineering. Adv Funct Mater 31(19):2009432. https://doi.org/10.1002/adfm.202009432
19. Yin Chin S, Cheung Poh Y, Kohler AC et al (2017) Additive manufacturing of hydrogel-based materials for next-generation implantable medical devices. Sci Robot 2(2):eaah6451. https://doi.org/10.1126/scirobotics.aah6451
20. Shahbazi M, Jäger H, Ettelaie R et al (2023) Multimaterial 3D printing of self-assembling smart thermo-responsive polymers into 4D printed objects: a review. Addit Manuf 71:103598.

https://doi.org/10.1016/j.addma.2023.103598
21. Maharjan B, Park J, Kaliannagounder VK et al (2021) Regenerated cellulose nanofiber reinforced chitosan hydrogel scaffolds for bone tissue engineering. Carbohydr Polym 251:117023. https://doi.org/10.1016/j.carbpol.2020.117023
22. Onofrillo C, Duchi S, Francis S et al (2021) FLASH: Fluorescently LAbelled Sensitive Hydrogel to monitor bioscaffolds degradation during neocartilage generation. Biomaterials 264: 120383. https://doi.org/10.1016/j.biomaterials.2020.120383
23. Rajalekshmi R, Kaladevi Shaji A, Joseph R et al (2021) Scaffold for liver tissue engineering: exploring the potential of fibrin incorporated alginate dialdehyde-gelatin hydrogel. Int J Biol Macromol 166:999–1008. https://doi.org/10.1016/j.ijbiomac.2020.10.256
24. Jiang HY, Fan LX, Yan S et al (2019) Tough and electro-responsive hydrogel actuators with bidirectional bending behavior. Nanoscale 11(5):2231–2237. https://doi.org/10.1039/c8nr07863g
25. Annabi N, Shin SR, Tamayol A et al (2016) Highly elastic and conductive human-based protein hybrid hydrogels. Adv Mater 28(1):40–49. https://doi.org/10.1002/adma.201503255
26. Wang XJ, Huang HQ, Liu H et al (2019) Multi-responsive bilayer hydrogel actuators with programmable and precisely tunable motions. Macromol Chem Phys 220(6):1800562. https://doi.org/10.1002/macp.201800562
27. Chen WN, Wen YB, Fan XJ et al (2021) Magnetically actuated intelligent hydrogel-based child-parent microrobots for targeted drug delivery. J Mater Chem B 9(4):1030–1039. https://doi.org/10.1039/D0TB02384A
28. Du XM, Cui HQ, Xu TT et al (2020) Reconfiguration, camouflage, and color-shifting for bioinspired adaptive hydrogel-based millirobots. Adv Funct Mater 30(10):1909202. https://doi.org/10.1002/adfm.201909202
29. Cao Y, Xu BG, Li B et al (2024) Advanced design of soft robots with artificial intelligence. Nanomicro Lett 16(1):214. https://doi.org/10.1007/s40820-024-01423-3
30. Xin C, Xia N, Zhang L (2024) Light-based 3D printing of stimulus-responsive hydrogels for miniature devices: recent progress and perspective. Bio-Des Manuf 7(5):721–746. https://doi.org/10.1007/s42242-024-00295-1
31. Yeom J, Choe A, Lim S et al (2020) Soft and ion-conducting hydrogel artificial tongue for astringency perception. Sci Adv 6(23):eaba5785. https://doi.org/10.1126/sciadv.aba5785
32. Chen Q, Yan M, Hu AN et al (2024) Injectable nanorobot-hydrogel superstructure for hemostasis and anticancer therapy of spinal metastasis. Nanomicro Lett 16(1):259. https://doi.org/10.1007/s40820-024-01469-3
33. Cao MM, Sheng RW, Sun YM et al (2024) Delivering microrobots in the musculoskeletal system. Nanomicro Lett 16(1):251. https://doi.org/10.1007/s40820-024-01464-8
34. Simińska-Stanny J, Nizioł M, Szymczyk-Ziółkowska P et al (2022) 4D printing of patterned multimaterial magnetic hydrogel actuators. Addit Manuf 49:102506. https://doi.org/10.1016/j.addma.2021.102506
35. Lavrador P, Esteves MR, Gaspar VM et al (2021) Stimuli-responsive nanocomposite hydrogels for biomedical applications. Adv Funct Mater 31(8):2005941. https://doi.org/10.1002/adfm.202005941
36. Wiesner SM, Decker SA, Larson JD et al (2009) *De novo* induction of genetically engineered brain tumors in mice using plasmid DNA. Cancer Res 69(2):431–439. https://doi.org/10.1158/0008-5472.CAN-08-1800
37. Wei W, Liu ZJ, Wang R et al (2010) Application of cine MRI in diagnosis and treatment of arachnoid cysts. Chin J Neurosurg 26(8):712–715 (in Chinese). https://doi.org/10.3760/cma.j.issn.1001-2346.2010.08.017
38. Chin EE, Zimmerman PT, Grant EG (2005) Sonographic evaluation of upper extremity deep venous thrombosis. J Ultrasound Med 24(6):829–838. https://doi.org/10.7863/jum.2005.24.6.829
39. Moore JE, Bertram CD (2018) Lymphatic system flows. Annu Rev Fluid Mech 50:459–482. https://doi.org/10.1146/annurev-fluid-122316-045259
40. Scheeres D, O'Brien W, Ponsky L et al (1990) Endoscopic stent configuration and bile flow rates in a variable diameter bile duct model. Surg Endosc 4(2):91–93. https://doi.org/10.1007/BF00591267
41. Worsøe J, Fynne L, Gregersen T et al (2011) Gastric transit and small intestinal transit time and motility assessed by a magnet tracking system. BMC Gastroenterol 11:145. https://doi.org/10.1186/1471-230X-11-145